nature geoscience

Article

https://doi.org/10.1038/s41561-024-01394-5

Detections of ultralow velocity zones in high-velocity lowermost mantle linked to subducted slabs

Received: 12 October 2022

Accepted: 7 February 2024

Published online: 4 March 2024

Check for updates

Yulong Su[1], Sidao Ni[2,3] ✉, Baolong Zhang[2,3], Yulin Chen[2,3], Wenbo Wu[4], Mingming Li[5], Heping Sun[2,3], Mingqiang Hou[2,3], Xiaoming Cui[2,3] & Daoyuan Sun[1]

Ultralow velocity zones revealed by seismological observations at the core–mantle boundary lend clues to the physico-chemical characteristics and dynamic evolution of the Earth's deep interior. Ultralow velocity zones have been primarily detected within and at the edges of the large low-velocity provinces. Ultralow velocity zones in high-velocity lowermost mantle have also been reported, but global assessment has been limited by data coverage. Here we use geophysical observations of the seismic phase SKKKP and its B-caustic diffractions (SKKKP waves beyond the B-caustic distance) for 60 large and deep-focus events recorded in North America, Europe and China to detect ultralow velocity zones at the core–mantle boundary. We analyse and simulate the extended SKKKP B-caustic diffractions with different velocity anomalies in the mantle and outer core. In addition to ultralow velocity zones around the two large low-velocity provinces beneath the mid-Pacific and Africa, our results support ultralow velocity zones in previously under-explored high-velocity lowermost mantle regions, including Central America, Alaska, Greenland and West and Central Asia. We suggest our evidence for ultralow velocity zones in high-velocity lowermost mantle is consistent with the presence of partially molten subducted oceanic crust at the deep lower mantle.

Seismological structures in the lowermost mantle are key to understanding mantle convection, core–mantle coupling and Earth's evolution. Multi-scale complex structures such as the large low-velocity provinces (LLVPs), high-velocity anomalies, ultralow velocity zones (ULVZs) and small-scale scatterers have been detected over the past decades[1,2]. As the most extreme features above the core–mantle boundary (CMB), ULVZs are characterized by reductions of P-wave and S-wave velocity up to 25% and 50%, with thicknesses ranging from several kilometres to 100 km, and lateral sizes ranging from tens of kilometres to 1,500 km (refs. 3,4).

Among various seismic probes, SKPdS[5,6] (or SPdKS) waves and PKP precursors[7,8] are widely used to investigate ULVZs above the CMB. Ni and Helmberger[9] used these two independent seismic phases to sample the same ULVZ structure beneath Central Africa and provided a strong constraint on the physical properties and morphology of that ULVZ. There are also many successful applications of the reflected core phases (PcP, ScS, ScP) in studying ULVZs via detailed modelling of their waveforms[10–12]. Moreover, the diffracted waves along the CMB have been used to detect ULVZs, including P_{diff}, S_{diff} and $PKKP_{diff}$[13,14].

[1]School of Earth and Space Sciences, University of Science and Technology of China, Hefei, China. [2]State Key Laboratory of Geodesy and Earth's Dynamics, Innovation Academy for Precision Measurement Science and Technology, Chinese Academy of Sciences, Wuhan, China. [3]College of Earth and Planetary Sciences, University of Chinese Academy of Sciences, Beijing, China. [4]Department of Geology and Geophysics, Woods Hole Oceanographic Institution, Woods Hole, MA, USA. [5]School of Earth and Space Exploration, Arizona State University, Tempe, AZ, USA. ✉e-mail: sdni@whigg.ac.cn

https://doi.org/10.1038/s41561-024-01394-5

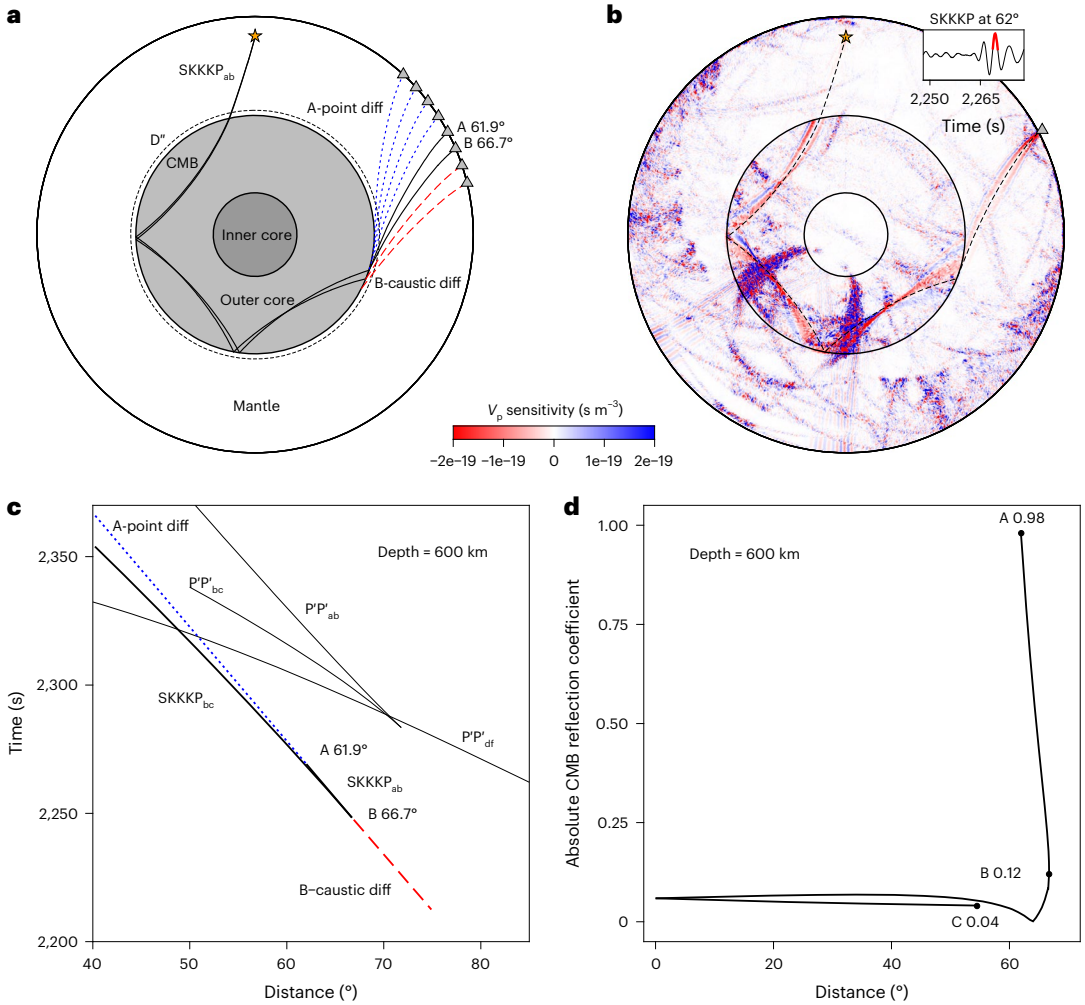

Fig. 1 | Basic information of SKKKP waves. a, Ray paths of SKKKP (solid black lines), SKKKP A-point diffractions (dotted blue lines) and SKKKP B-caustic diffractions (dashed red lines) from the source (orange star) to the receivers (grey triangles). **b**, Delay-time sensitivity kernel of SKKKP to P-wave velocity (V_p) at an epicentral distance of 62°. The dashed black line shows the ray path of SKKKP. The waveform segment used for sensitivity kernel calculation is marked by a red line in the inset. **c**, Travel time versus epicentral distance curves for SKKKP (thick solid black lines), SKKKP A-point diffractions (dotted blue line), SKKKP B-caustic diffractions (dashed red line) and P′P′ (thin solid black lines). **d**, Reflection coefficient versus epicentral distance curve for SKKKP at the underside of the CMB. In **a** and **c**, 'diffractions' is simplified to 'diff'. All the theoretical values are calculated with a source depth of 600 km in the AK135 model.

With these core phases, researchers have revealed ULVZs that are primarily located near and within the LLVPs[3,4,15], with some beneath hotspots[16–18]. ULVZs are also detected in high-velocity lowermost mantle regions that appear to be associated with subducted materials[5,19,20]. However, due to the limited spatial distribution of earthquakes and stations, the path coverage for the high-velocity lowermost mantle is insufficient.

Expanding the path coverage with more seismic phases is essential for better characterizing ULVZs globally. The seismic core phase SKKKP is a down-going S wave that converts to a P wave (K) in the liquid outer core, reflects twice at the underside of the CMB and propagates as a P wave in the mantle after exiting the outer core (Fig. 1a,b). There are two branches of SKKKP bottoming in the outer core (denoted as SKKKP$_{ab}$ and SKKKP$_{bc}$). According to classical ray theory, the epicentral distance range of the ab branch for a source depth of 600 km in the AK135 model[21] is 61.9–66.7° (minor arc, or 293.3–298.1°, if major arc distance is used). Like other multiply reflected core phases (such as PKKP[14]), SKKKP waves may propagate beyond the A-point distance (less than 61.9°) due to the diffraction effects along the CMB (denoted as SKKKP A-point diffractions). There are also SKKKP waves that propagate beyond the B-caustic distance (greater than 66.7°) in our observations, and we refer to them as SKKKP B-caustic diffractions (Fig. 1a,c).

In this study, we propose that SKKKP B-caustic diffractions can provide another effective tool for detecting ULVZs. We explored a global dataset of SKKKP B-caustic diffractions by analysing the characteristics of candidate waveforms from large, deep-focus events recorded by dense arrays. Combining seismic observations and forward modelling of the extended SKKKP B-caustic diffractions, we suggest ULVZs in several high-velocity lowermost mantle regions and some around two LLVPs. The distributions of ULVZs in high-velocity lowermost support that they are related to former subducted slabs.

Characteristics of SKKKP and its B-caustic diffractions

SKKKP is a multiply reflected core phase, with the reflection coefficient of the A-point distance substantially larger than the B-caustic distance at the underside of the CMB (Fig. 1d). However, the focusing effects near the B-caustic distance could compensate for the low reflection coefficient, making SKKKP B-caustic diffractions observable. Chen et al.[22] reported that PKKP A-point diffractions mainly occur near the mantle side of their core entry and exit regions. Nevertheless, the mechanisms behind B-caustic diffractions and the significance of their extension length (the length of waves beyond the B-caustic distance) remain unclear. Here we calculated the sensitivity kernels for SKKKP waves in

https://doi.org/10.1038/s41561-024-01394-5

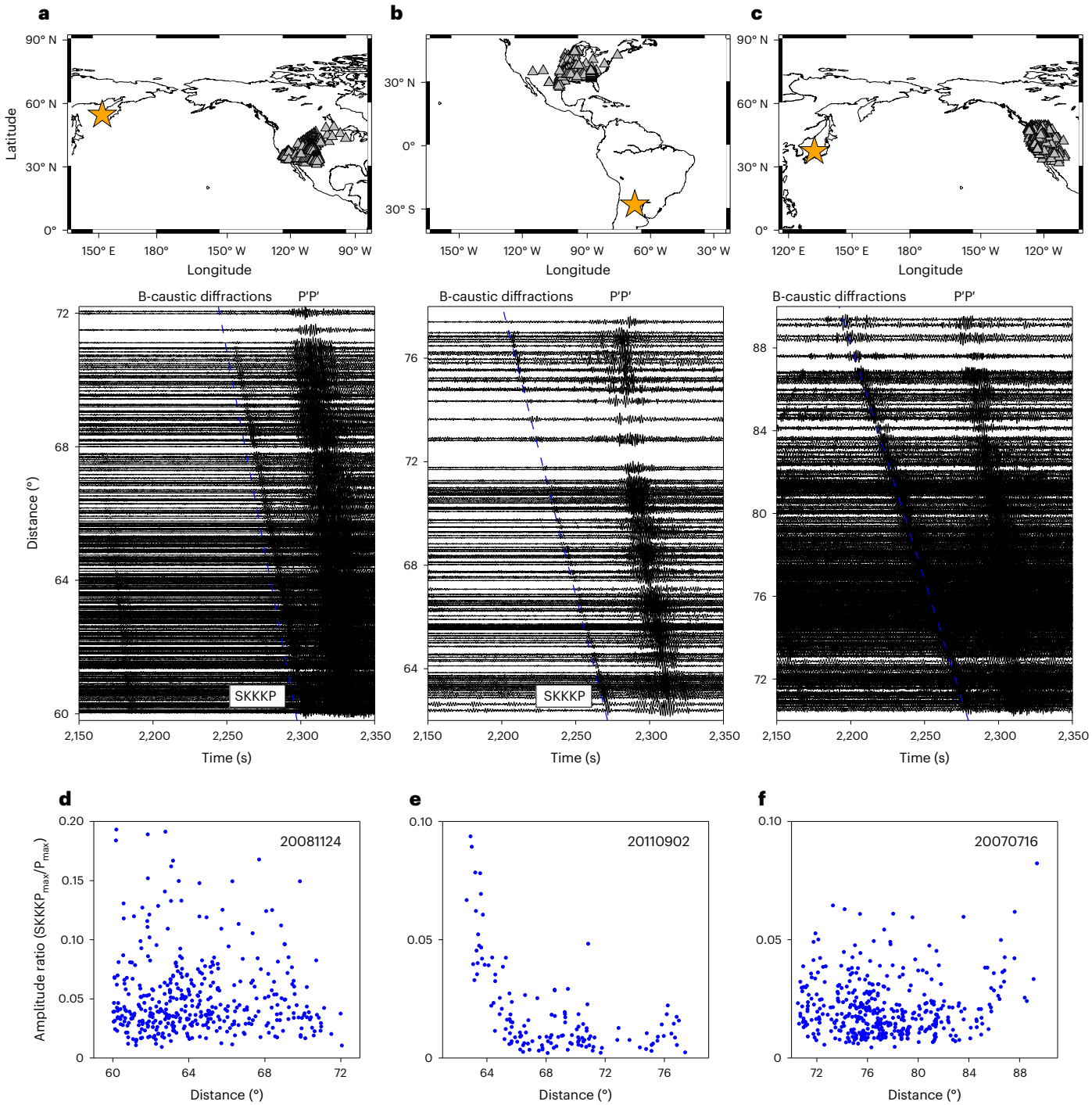

Fig. 2 | Three examples of seismograms that show SKKKP and its B-caustic diffractions along with P'P'. **a**–**c**, Record sections show vertical component seismograms in the frequency band 0.5–1.2 Hz for three deep-focus events. **a**, The 20081124 event, magnitude M_b 6.5, depth 490.7 km. **b**, The 20110902 event, magnitude M_b 6.4, depth 592.7 km. **c**, The 20070716 event, magnitude M_b 6.2, depth 358.2 km. The dashed blue lines show the theoretical travel time curves of SKKKP and its B-caustic diffractions calculated with the AK135 model using a constant slowness of −4.37 s per deg. The maps above the record sections show the locations of events (orange stars) and stations (grey triangles). **d**–**f**, Amplitude ratio of SKKKP$_{max}$/P$_{max}$ versus epicentral distance for the three events in **a**–**c**.

the distance range of 58–70° using the MC Kernel[23] (Fig. 1b and Supplementary Fig. 1). The wavefield databases were generated at a dominant period of 4 s with the AK135 model for practicable storage and input/output costs. The kernels exhibit high sensitivities in the outer core region, followed by the source-side and receiver-side regions, but negligible sensitivities on the mantle side of two CMB underside reflection regions. Moreover, SKKKP waves display a broader sensitivity range and higher P-wave velocity kernel values near the mantle side of their core exit region compared with core entry region. The broader sensitivity range of SKKKP waves near the core exit region may facilitate the occurrence of both A-point diffractions and B-caustic diffractions, if the corresponding regions have heterogeneities that affect seismic wave propagation. Previous studies have mainly focused on the A-point diffractions of seismic core phases and successfully revealed anomalous

https://doi.org/10.1038/s41561-024-01394-5

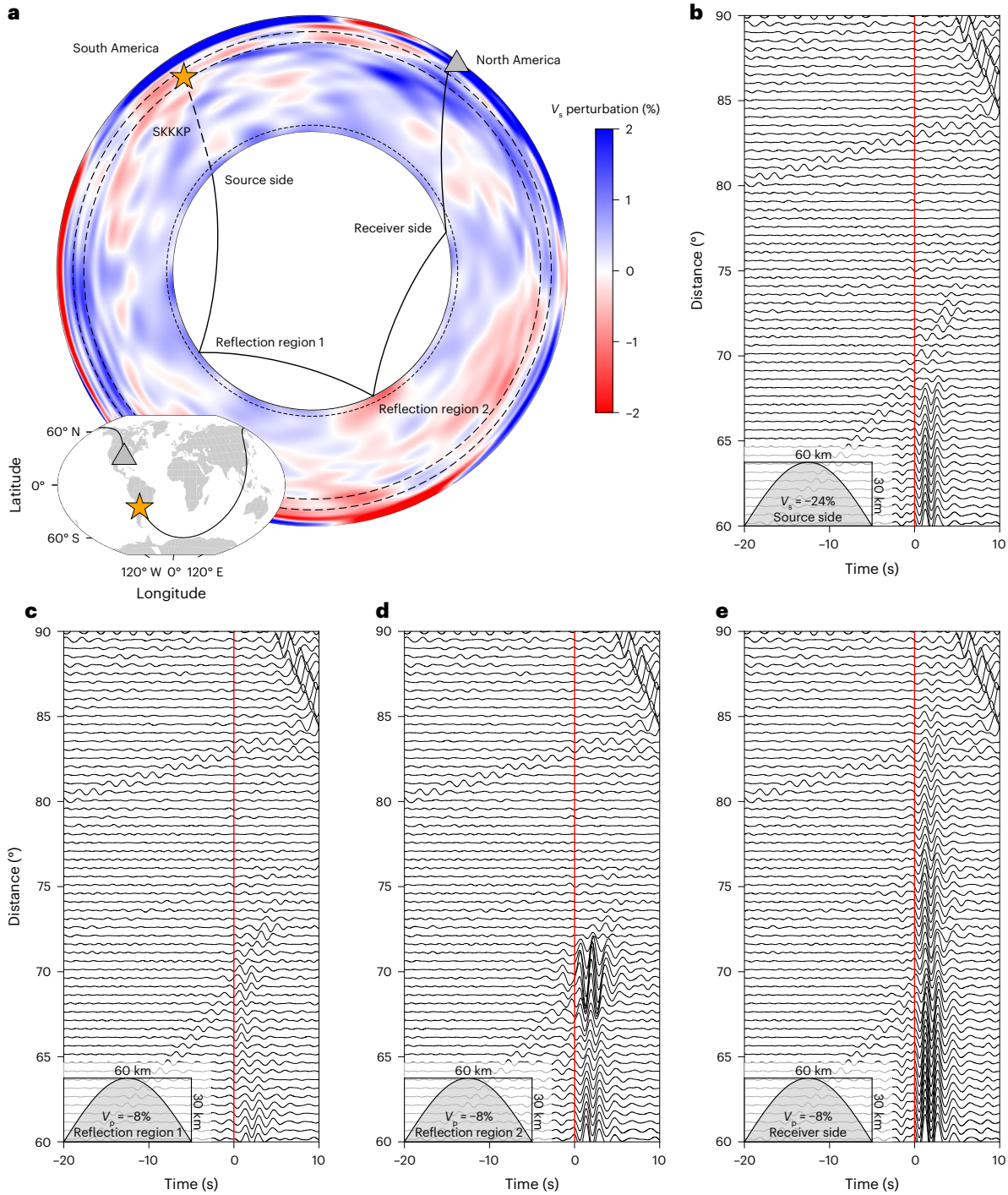

Fig. 3 | Synthetic seismograms for 2D ULVZ models at four CMB interaction regions of SKKKP. a, SKKKP ray path (black line) through the depth cross-section of the S-wave velocity (V_s) tomographic model S40RTS along the source (orange star) and receiver (grey triangle) azimuth of the 20110902 event (black path in the inset). **b**–**e**, Synthetic seismograms for a single sinusoid-shaped ULVZ model with a thickness of 30 km, a width of 60 km and a S-wave velocity reduction of 24% at the source side (**b**) or a P-wave velocity reduction of 8% at reflection region 1 (**c**), reflection region 2 (**d**) and receiver side (**e**). The seismic phase at the top right corner is pPKPPcP. All the waveforms are aligned with the theoretical arrival times of SKKKP and its B-caustic diffractions (red lines) and filtered with 0.5–1.0 Hz.

features in the Earth's deep interior. B-caustic diffractions are equally important for exploring the structures near the CMB, awaiting more detailed studies.

With the increasing number of seismic stations, more high-quality waveform data become available for better studying this promising seismic phase that has not yet been well explored. The details about our observations are given in the Methods (Extended Data Figs. 1 and 2 and Supplementary Tables 1–4). Figure 2a–c shows SKKKP and its B-caustic diffractions in the frequency band 0.5–1.2 Hz from three earthquakes with maximum extension length of 6°, 12° and 24°, respectively. The theoretical arrival time of SKKKP is calculated with the AK135 model. For the B-caustic diffractions, we used the formula $t = t_B - 4.37$ s per degree (deg) × Δd, where t_B and −4.37 s per deg are the arrival time and slowness at the B-caustic distance and Δd is the extension length.

https://doi.org/10.1038/s41561-024-01394-5

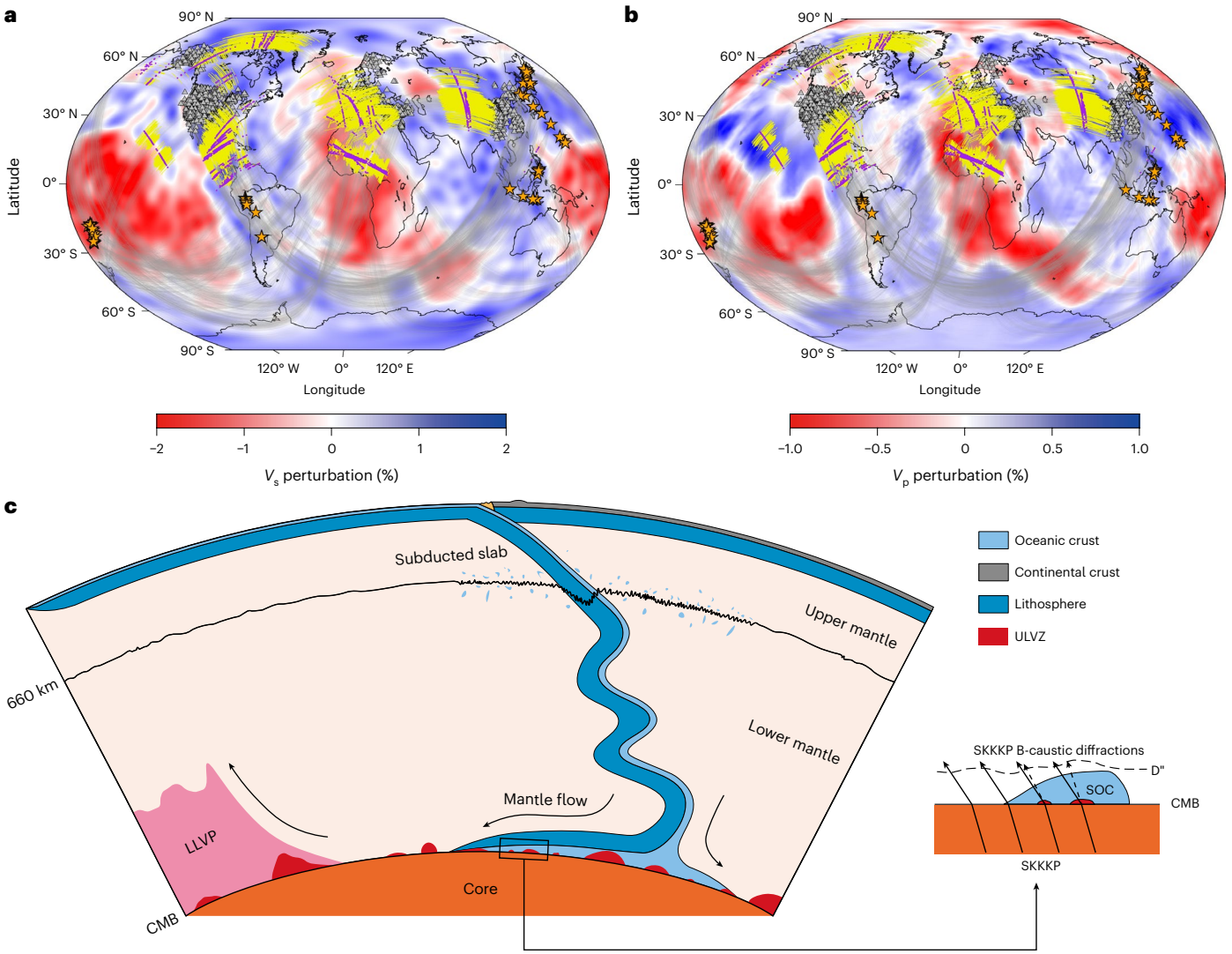

Fig. 4 | Sampling regions of SKKKP B-caustic diffractions and dynamic processes of ULVZ evolution. a,**b**, Locations of the sampling regions. Events (orange stars) and stations (grey triangles) are connected by great circle paths (grey lines). Yellow lines indicate the potential sampling regions of SKKKP B-caustic diffractions at the CMB, and their lengths represent the extension lengths. The purple points represent the theoretical core exit point of SKKKP at B-caustic distance for event–station pairs. The background models display the S-wave velocity perturbations (**a**) from the S40RTS at a depth of 2,850 km and P-wave velocity perturbations (**b**) from the LLNL-G3Dv3 at a depth of 2,870 km. **c**, Schematic diagram of ULVZs in high-velocity lowermost mantle. The subducted oceanic crust (SOC) is partially molten due to the chemical differences and temperature perturbations near the CMB; then the partially molten materials could be pushed by mantle flow to the edges of the LLVP. The inset shows a magnified area of the black box in **c**; the solid black lines show the ray paths of SKKKP and the dashed black lines show SKKKP B-caustic diffractions.

From Fig. 2a–c, we found that the signals are almost coincident with the theoretical travel time curves, indicating that they are consistent with SKKKP and its B-caustic diffractions. We also measured the amplitude ratios of $SKKKP_{max}/P_{max}$ for the three events; the relative amplitude could mitigate the influence of the shallow structures beneath stations. Figure 2d–f shows that the amplitude ratios decrease with increasing extension lengths but with substantial scatter. Similar rapid variations of short-period body waves have been observed and are proposed to be related to small-scale heterogeneities[24]. Moreover, it can be noticed that the amplitude ratios in Fig. 2e follow an exponential decay, but this feature is not applicable to most events.

We also measured the polarization, frequency, particle motion, slowness and back azimuth of these signals to further analyse the characteristics of SKKKP and its B-caustic diffractions (Extended Data Figs. 3 and 4, Supplementary Figs. 2–6 and Methods). However, the ray theoretical SKKKP B-caustic distance range in the AK135 model is 66–67°, whereas the SKKKP B-caustic diffractions can be observed up to 98° in our observations, implying very anomalous structures in the Earth's interior that cause the long-distance extension.

Correlations with anomalous seismic structures

SKKKP propagates through the crust, mantle and outer core and thus could be affected by the complexities that exist in these layers of the Earth. The small-scale heterogeneities in the crust and mantle are widely distributed and can cause strong scattering of seismic waves[1]. However, our analyses show that SKKKP B-caustic diffractions mainly propagate along the great circle path and their slowness is nearly constant (Extended Data Fig. 4 and Supplementary Fig. 6), so it is difficult to explain the observations with random scatterers. According to Buchbinder[25], the B-caustic distance for PmKP (m = 3, 4, 5, 6 and 7 represents the number of reflections at the underside of the CMB) can be shifted if the velocity around their turning points in the outer core is increased, but the liquid outer core is highly dynamic with negligible

lateral variations due to the low viscosity, which is unlikely to generate the long-distance extension of SKKKP B-caustic diffractions.

Anomalies related to large-scale mantle structures, such as sharp edges of LLVPs[26] and velocity anomalies within slabs[27], may generate anomalous waveforms contributing to SKKKP B-caustic diffractions. Extended Data Fig. 1 shows that SKKKP B-caustic diffractions recorded by stations in the Europe region could be influenced by the LLVP beneath Africa. Therefore, we tested the effects of LLVP sharp edges on SKKKP waves in three scenarios (Supplementary Fig. 7). The LLVP model is sinusoid shaped with a height of 1,200 km, a width of 3,600 km and a P-wave velocity reduction of 2%. The results show that SKKKP waves propagating over longer distances within the LLVP exhibit later arrival times, whereas SKKKP waves interacting extensively with the LLVP edges exhibit weaker amplitudes due to the scattering effects[13] (Supplementary Fig. 8). However, the SKKKP B-caustic diffractions are not pronounced in the seismograms. It is also worth noting that partial SKKKP ray paths in our observations do not pass through LLVPs, so the sources of SKKKP B-caustic diffractions are more likely from some widespread heterogeneities.

We also tested the effects of velocity anomalies within slabs on SKKKP waves using a 3D hybrid method with different slab structure models (Extended Data Fig. 5). The set-up of 3D models is described in the Methods. Our results show that velocity anomalies within the slabs do impact the SKKKP waveform. For instance, the presence of a low-velocity zone in the first model delays the arrival times of SKKKP compared with the other two models. However, the influence on the distance extension of SKKKP B-caustic diffractions is not notable (Supplementary Fig. 9). Considering the uncertainties associated with the source depth and the Slab2 model[28], which may influence the slab structure effects, we conducted additional tests by varying the depth of the earthquake while maintaining the low-velocity oceanic crust model (Extended Data Fig. 6). Despite these variations, our conclusion remains consistent; no notable effects were observed on the distance extension of SKKKP B-caustic diffractions.

The last scenario focuses on the anomalous structures near the CMB. We performed a series of modelling experiments around the CMB region to investigate the causes of the extended SKKKP B-caustic diffractions (Methods and Supplementary Information). Tests show that 1D anomalous velocity structures near the CMB do not significantly affect the extended SKKKP B-caustic diffractions (Extended Data Table 1, Supplementary Figs. 10–13 and Supplementary Information). Therefore, the long-distance extension of SKKKP B-caustic diffractions is most likely attributed to highly lateral heterogeneities near the CMB. Our calculations also show that the CMB topography has limited influence on SKKKP B-caustic diffractions, as a very large topography (5 km) only extends to 75° (Supplementary Fig. 14). Another important structure, ULVZs, has been demonstrated to be widespread along the CMB, accompanied by strong lateral heterogeneity[3,20]. Thus, we calculated synthetic seismograms for 2D ULVZ models with typical parameters at four CMB interaction regions of SKKKP (Fig. 3 and Supplementary Table 5). The ULVZ models are sinusoid shaped with a thickness of 30 km, a width of 60 km and a P-wave velocity reduction of 8% (or a S-wave velocity reduction of 24%, considering that SKKKP on the source side is a shear wave). We found that the ULVZ model on the source side does not generate the extended SKKKP B-caustic diffractions (Fig. 3b). We also tested ULVZ models with 8% P-wave velocity reduction or larger size and velocity reduction on the source side (Supplementary Fig. 15), but similarly, the SKKKP B-caustic diffractions do not extend in the synthetics. Secondly, setting a ULVZ model on the mantle side of CMB underside reflection regions of SKKKP affects the reflection coefficient, resulting in obvious variations of SKKKP amplitude but with minimal impact on extension length (Fig. 3c,d). While setting a ULVZ model on the receiver side, SKKKP B-caustic diffractions extend to 80° in the synthetics (Fig. 3e), which is consistent with the observations shown in Fig. 2. In addition, the B-caustic diffractions are more observable at higher frequencies due to avoiding the interference from other long-period phases (Supplementary Fig. 16), consistent with the high-frequency characteristic in observations.

Our synthetic seismograms support that the extended SKKKP B-caustic diffractions in observations can be attributed to ULVZ structures at SKKKP core exit locations, although we do not exclude other unusual structures that may contribute to some portion of the extended energy. To further understand the impact of various ULVZ parameters on SKKKP B-caustic diffractions, we tested a set of 2D ULVZ models with different shape, number, location, P-wave velocity reduction, thickness and width (Extended Data Table 2, Supplementary Figs. 17–20 and Methods). For example, synthetic results show that SKKKP B-caustic diffractions are most sensitive to the P-wave velocity reduction of the modelled ULVZs (Extended Data Fig. 7). Another anomalous issue is the variable amplitude of SKKKP signals. Among the 143 events, SKKKP and its B-caustic diffractions are not observed for 83 events. On the other hand, we noticed that the amplitudes of SKKKP in several events are nearly an order of magnitude larger than the synthetic predictions. Through tests, we attributed the variable amplitude to various factors, such as noise levels, source parameter errors, anomalous mantle structures and quality factors of the lower mantle (Supplementary Figs. 21 and 22, Supplementary Tables 6 and 7 and Supplementary Information).

Dynamic evolution of ULVZs in high-velocity lowermost mantle

For the 60 events with observable SKKKP B-caustic diffractions, we plotted the sampling regions along the CMB and compared them with S-wave[29–31] and P-wave[32,33] velocity tomographic models in the lowermost mantle. These SKKKP B-caustic diffractions sample several regions at the CMB, including some high-velocity lowermost mantle regions beneath Central America, Alaska, Greenland, West and Central Asia and the regions around the northeastern Pacific LLVP and northern African LLVP (Fig. 4a,b and Extended Data Fig. 8). Many studies have detected ULVZs near the northeastern Pacific LLVP[10,11,13,34] and Central America[5,35] (Supplementary Fig. 23). The regions beneath northern African LLVP and West and Central Asia have also been implicated for ULVZs in a few previous studies[3,6]. However, our sampling regions are generally unexplored for ULVZ structures, mainly due to the limited source–receiver geometries (Methods discusses ULVZ properties in high-velocity lowermost mantle regions).

The locations of ULVZs may indicate their origins and dynamic processes. Previous studies have suggested that the partial melt origin of ULVZs could explain the 1:3 ratio in P-wave to S-wave velocity reduction and the correlation between ULVZs and hotspots[16,17]. These ULVZs are primarily influenced by thermal anomalies and are located at the hottest lowermost mantle regions, commonly occurring within the interior of LLVPs[36]. ULVZs near the edges of the LLVPs or in high-velocity lowermost mantle may be better explained by the compositionally distinct origin[36–38]. Several hypotheses have invoked chemical anomalies to account for these ULVZs. Recent high pressure and temperature experiments propose that a thin core rigidity zone underside the mantle could provide compositionally distinct materials[39]. Nonetheless, the processes by which core rigidity zone materials are incorporated into the mantle remain unclear and warrant further investigation by geodynamic studies. Another possible explanation for compositionally distinct ULVZs is that they are iron-enriched remnants of the crystallization of basal magma ocean. These remnants would have already been dragged by the long-term mantle flow and resided at the edges of the LLVPs[12,36,40].

Alternatively, mineral physics experiments suggest that compositional anomalies at the CMB may originate from subducted materials[41–43]. A recent study, combining seismological data with geodynamic modelling, further suggests that the base of the mantle contains globally distributed subducted materials with variable concentrations of

subducted oceanic crust[20]. Using the unique ray path of SKKKP phase, we present seismic indications for ULVZs in several high-velocity lowermost mantle regions. These regions have been proposed to be strongly influenced by subduction processes[2,44]. In addition, previous studies have found evidence of remnants of oceanic plates that were subducted to the CMB beneath Central America, Alaska, West and Central Asia[45], indicating that ULVZs in our observations are associated with former subducted slabs (Fig. 4c).

Subducted slabs consist of a thinner oceanic crust (6–7 km) and a thicker underlying mantle lithosphere. Once arriving at the base of the mantle, cold subducted slabs could perturb the thermal structure in this region and induce the formation of small-scale hot thermal anomalies on the CMB[46]. Geodynamic modelling experiments have shown subducted oceanic crust in the lowermost mantle could segregate from the slabs and fall on the CMB[47–49] (Fig. 4c). As suggested by mineral physics experiments, subducted oceanic crust has a relatively low melting temperature[43]. Therefore, it could be partially molten on the CMB, especially when it is transported to hot thermal anomalies, as suggested by Li[46]. The partially molten subducted oceanic crust is expected to migrate along the CMB from subduction-related downwelling areas to the edges of the LLVPs[20,48,50] (Fig. 4c). Therefore, ULVZs in our sampling regions both in high-velocity lowermost mantle and near LLVPs can be attributed to subducted oceanic crust.

Our findings imply that ULVZs detected by previous studies may also be related to subducted oceanic crust, although other mechanisms may contribute to the formation of some ULVZs above the CMB, such as remnants of magma ocean crystallization[40]. However, it seems that SKKKP B-caustic diffractions are mainly sensitive to P-wave velocity reduction on the receiver side and do not provide tight constraints on S-wave velocity (Supplementary Fig. 24); thus, the interpretation of ULVZs with molten materials from former subducted slabs requires further evidence from S-wave velocity and density modelling. Future efforts should obtain more observations to further explore the distribution and multiple seismic parameters of ULVZs so as to promote a comprehensive understanding of the origins and dynamic processes of ULVZs.

Online content

Any methods, additional references, Nature Portfolio reporting summaries, source data, extended data, supplementary information, acknowledgements, peer review information; details of author contributions and competing interests; and statements of data and code availability are available at https://doi.org/10.1038/s41561-024-01394-5.

References

1. Hedlin, M. A., Shearer, P. M. & Earle, P. Seismic evidence for small-scale heterogeneity throughout the Earth's mantle. *Nature* **387**, 145–150 (1997).
2. Garnero, E. J. & McNamara, A. K. Structure and dynamics of Earth's lower mantle. *Science* **320**, 626–628 (2008).
3. Yu, S. & Garnero, E. J. Ultralow velocity zone locations: A global assessment. *Geochem. Geophys. Geosyst.* **19**, 396–414 (2018).
4. Li, J., Sun, D. & Bower, D. J. Slab control on the mega-sized North Pacific ultra-low velocity zone. *Nat. Commun.* **13**, 1042 (2022).
5. Thorne, M. S., Takeuchi, N. & Shiomi, K. Melting at the edge of a slab in the deepest mantle. *Geophys. Res. Lett.* **46**, 8000–8008 (2019).
6. Thorne, M. S. et al. The most parsimonious ultralow-velocity zone distribution from highly anomalous SPdKS waveforms. *Geochem. Geophys. Geosyst.* **22**, e2020GC009467 (2021).
7. Wen, L. & Helmberger, D. V. Ultra-low velocity zones near the core-mantle boundary from broadband PKP precursors. *Science* **279**, 1701–1703 (1998).
8. Ma, X., Sun, X. & Thomas, C. Localized ultra-low velocity zones at the eastern boundary of Pacific LLSVP. *Earth Planet. Sci. Lett.* **507**, 40–49 (2019).
9. Ni, S. & Helmberger, D. V. Probing an ultra-low velocity zone at the core mantle boundary with P and S waves. *Geophys. Res. Lett.* **28**, 2345–2348 (2001).
10. Mori, J. & Helmberger, D. V. Localized boundary layer below the mid-Pacific velocity anomaly identified from a PcP precursor. *J. Geophys. Res.* **100**, 20359–20365 (1995).
11. Lay, T., Hernlund, J., Garnero, E. J. & Thorne, M. S. A post-perovskite lens and D″ heat flux beneath the Central Pacific. *Science* **314**, 1272–1276 (2006).
12. Pachhai, S., Li, M., Thorne, M. S., Dettmer, J. & Tkalčić, H. Internal structure of ultralow-velocity zones consistent with origin from a basal magma ocean. *Nat. Geosci.* **15**, 79–84 (2022).
13. Kim, D., Lekić, V., Ménard, B., Baron, D. & Taghizadeh-Popp, M. Sequencing seismograms: A panoptic view of scattering in the core-mantle boundary region. *Science* **368**, 1223–1228 (2020).
14. Rost, S. & Garnero, E. J. Detection of an ultralow velocity zone at the core-mantle boundary using diffracted PKKPab waves. *J. Geophys. Res. Solid Earth* **111**, B07309 (2006).
15. Cottaar, S. & Romanowicz, B. An unsually large ULVZ at the base of the mantle near Hawaii. *Earth Planet. Sci. Lett.* **355–356**, 213–222 (2012).
16. Williams, Q., Revenaugh, J. & Garnero, E. J. A correlation between ultra-low basal velocities in the mantle and hot spots. *Science* **281**, 546–549 (1998).
17. Rost, S., Garnero, E. J., Williams, Q. & Manga, M. Seismological constraints on a possible plume root at the core–mantle boundary. *Nature* **435**, 666–669 (2005).
18. Li, Z., Leng, K., Jenkins, J. & Cottaar, S. Kilometer-scale structure on the core-mantle boundary near Hawaii. *Nat. Commun.* **13**, 2787 (2022).
19. Yao, J. & Wen, L. Seismic structure and ultra-low velocity zones at the base of the Earth's mantle beneath Southeast Asia. *Phys. Earth Planet. Inter.* **233**, 103–111 (2014).
20. Hansen, S. E., Garnero, E. J., Li, M., Shim, S.-H. & Rost, S. Globally distributed subducted materials along the Earth's core-mantle boundary: Implications for ultralow velocity zones. *Sci. Adv.* **9**, eadd4838 (2023).
21. Kennett, B. L. N., Engdahl, E. R. & Buland, R. Constraints on seismic velocities in the Earth from traveltimes. *Geophys. J. Int.* **122**, 108–124 (1995).
22. Chen, Y. et al. Sensitivities of diffracted PKKPab waves to the velocity structures in the lowermost mantle. *Geophys. J. Int.* **233**, 1617–1631 (2023).
23. Stähler, S. C. et al. MC kernel: broadband waveform sensitivity kernels for seismic tomography. *Geophys. Res. Abstr.* **18**, EGU2016-7020-2 (2016).
24. Ruff, L. J. & Helmberger, D. V. The structure of the lowermost mantle determined by short-period P-wave amplitudes. *Geophys. J. Int.* **68**, 95–119 (1982).
25. Buchbinder, G. G. R. Travel times and velocities in the outer core from PmKP. *Earth Planet. Sci. Lett.* **14**, 161–168 (1972).
26. To, A., Romanowicz, B., Capdeville, Y. & Takeuchi, N. 3D effects of sharp boundaries at the borders of the African and Pacific superplumes: observation and modelling. *Earth Planet. Sci. Lett.* **233**, 1447–1460 (2005).
27. Audet, P., Bostock, M. G., Christensen, N. I. & Peacock, S. M. Seismic evidence for overpressured subducted oceanic crust and megathrust fault sealing. *Nature* **457**, 76–78 (2009).
28. Hayes, G. P. et al. Slab2, a comprehensive subduction zone geometry model. *Science* **362**, 58–61 (2018).
29. Ritsema, J., Deuss, A., van Heijst, H. J. & Woodhouse, J. H. S40RTS: a degree-40 shear-velocity model for the mantle from new Rayleigh wave dispersion, teleseismic traveltime and normal-mode splitting function measurements. *Geophys. J. Int.* **184**, 1223–1236 (2011).

30. Simmons, N. A., Forte, A. M., Boschi, L. & Grand, S. P. GyPSuM: A joint tomographic model of mantle density and seismic wave speeds. *J. Geophys. Res. Solid Earth* **115**, B12310 (2010).
31. French, S. W. & Romanowicz, B. A. Whole-mantle radially anisotropic shear velocity structure from spectral-element waveform tomography. *Geophys. J. Int.* **199**, 1303–1327 (2014).
32. Simmons, N. A., Myers, S. C., Johannesson, G. & Matzel, E. LLNL-G3Dv3: global P wave tomography model for improved regional and teleseismic travel time prediction. *J. Geophys. Res. Solid Earth* **117**, B10302 (2012).
33. Li, C., van der Hilst, R. D., Engdahl, E. R. & Burdick, S. A new global model for P wave speed variations in Earth's mantle. *Geochem. Geophys. Geosyst.* **9**, Q05018 (2008).
34. Zhao, C. P., Garnero, E. J., Li, M. M., McNamara, A. & Yu, S. L. Intermittent and lateral varying ULVZ structure at the northeastern margin of the Pacific LLSVP. *J. Geophys. Res. Solid Earth* **122**, 1198–1220 (2017).
35. Niu, F. & Wen, L. Strong seismic scatterers near the core–mantle boundary West of Mexico. *Geophys. Res. Lett.* **28**, 3557–3560 (2001).
36. Li, M., McNamara, A. K., Garnero, E. J. & Yu, S. Compositionally-distinct ultra-low velocity zones on Earth's core–mantle boundary. *Nat. Commun.* **8**, 177 (2017).
37. McNamara, A. K., Garnero, E. J. & Rost, S. Tracking deep mantle reservoirs with ultra-low velocity zones. *Earth Planet. Sci. Lett.* **299**, 1–9 (2010).
38. Mao, W. L. et al. Iron-rich post-perovskite and the origin of ultralow-velocity zones. *Science* **312**, 564–565 (2006).
39. Fu, S., Chariton, S., Prakapenka, V. B. & Shim, S.-H. Core origin of seismic velocity anomalies at Earth's core–mantle boundary. *Nature* **615**, 646–651 (2023).
40. Labrosse, S., Hernlund, J. W. & Coltice, N. A crystallizing dense magma ocean at the base of the Earth's mantle. *Nature* **450**, 866–869 (2007).
41. Dobson, D. P. & Brodholt, J. P. Subducted banded iron formations as a source of ultralow-velocity zones at the core-mantle boundary. *Nature* **434**, 371–374 (2005).
42. Liu, J., Li, J., Hrubiak, R. & Smith, J. S. Origins of ultralow velocity zones through slab-derived metallic melt. *Proc. Natl Acad. Sci. USA* **113**, 5547–5551 (2016).
43. Andrault, D. et al. Melting of subducted basalt at the core-mantle boundary. *Science* **344**, 892–895 (2014).
44. van der Hilst, R., Widiyantoro, S. & Engdahl, E. Evidence for deep mantle circulation from global tomography. *Nature* **386**, 578–584 (1997).
45. van der Meer, D. G., van Hinsbergen, D. J. J. & Spakman, W. Atlas of the underworld: slab remnants in the mantle, their sinking history, and a new outlook on lower mantle viscosity. *Tectonophysics* **723**, 309–448 (2018).
46. Li, M. The formation of hot thermal anomalies in cold subduction-influenced regions of Earth's lowermost mantle. *J. Geophys. Res. Solid Earth* **125**, e2019JB019312 (2020).
47. Tackley, P. J. Living dead slabs in 3-D: The dynamics of compositionally-stratified slabs entering a 'slab graveyard' above the core–mantle boundary. *Phys. Earth Planet. Inter.* **188**, 150–162 (2011).
48. Li, M. in *Mantle Convection and Surface Expressions* (eds Marquardt, H. et al.) 303–328 (American Geophysical Union, 2021).
49. Li, M. Variable distribution of subducted oceanic crust beneath subduction regions of the lowermost mantle. *Phys. Earth Planet. Inter.* **341**, 107063 (2023).
50. Li, M. & McNamara, A. K. Evolving morphology of crustal accumulations in Earth's lowermost mantle. *Earth Planet. Sci. Lett.* **577**, 117265 (2022).

Methods

Data processing and analyses

We analysed the observations of SKKKP and its B-caustic diffractions recorded by dense arrays in North America, Europe and China. These seismic arrays have relatively small interstation spacing and can provide broad geographic coverage. We specifically selected earthquakes with depths greater than 300 km to mitigate the influence of lithospheric and asthenosphere structures. Moreover, to observe sufficiently strong SKKKP waves, earthquakes with magnitude greater than M_b 6.0 were selected. Then, we collected broad-band and short-period seismic recordings with epicentral distance range of 60–100° from 143 events occurring between 2000 and 2020. Most of these earthquakes are located in South America and the western Pacific (Extended Data Fig. 1). The raw waveform data were then pre-processed, including demeaning, detrending, tapering, removing the instrument response to obtain ground displacement and rotating to the great circle path.

We compared the three-component record sections of the suspect SKKKP signals along with P′P′ waves (Supplementary Fig. 2). Both seismic phases show the largest amplitude on the vertical component seismogram, confirming that the signals are also a type of P phase. The frequency characteristic is also important for identifying seismic phases. By filtering with different frequency bands, we found that the SKKKP signals have a relatively high-frequency content (Supplementary Fig. 3). Because the signals have higher signal-to-noise ratio in the frequency band 0.5–1.2 Hz (Supplementary Fig. 4), we adopted this frequency band for subsequent analyses.

Subsequently, we performed further screening to identify high-quality vertical component waveform data using the following steps. (1) We discarded events that do not show SKKKP waves. (2) We eliminated events that were contaminated by direct phases or coda waves of other earthquakes. (3) For events showing observable SKKKP waves, we only retained the seismograms with a $SKKKP_{max}/Noise_{max}$ greater than 1.5. Here $Noise_{max}$ is defined as the maximum amplitude of seismograms in the time window 10–60 seconds before SKKKP signals. (4) We conducted a visual examination of all the seismograms and removed the traces exhibiting unclear SKKKP waves. After applying these screening criteria, we retained 60 events with 7,918 seismograms of SKKKP waves (among them, 4,911 seismograms are B-caustic diffractions), and the source depths of these events are mostly greater than 550 km (42 events).

Slowness and back azimuth measurements

Slowness measurement is a critical tool for distinguishing SKKKP B-caustic diffractions from P′P′ precursors that result from the reflection of P′P′ waves at upper mantle interfaces[51] (denoted as P′dP′). The arrival times of P′dP′ might be close to SKKKP B-caustic diffractions, but their slownesses are different. The slowness of $P'P'_{df}$ is smaller than 2 s per deg, and the slownesses of $P'P'_{ab}$ and $P'P'_{bc}$ are smaller than 4.2 s per deg. Because the ray paths of P′dP′ are close to P′P′ waves, their slownesses are similar. In contrast, the slownesses of SKKKP and its B-caustic diffractions are greater than 4.2 s per deg.

To better analyse the characteristic of slowness, we used SKKKP waves recorded by Southern California Seismic Network (SCSN). This seismic network is suitable for measuring the slowness of weak signals because of its high-quality waveforms and dense stations. Extended Data Fig. 3 shows five examples of seismograms in the SKKKP time window recorded by SCSN at different distance ranges. For each event, we plotted the particle motions at the station with high signal-to-noise ratio and found that their motion directions are nearly vertical, which further confirms that the signals are a type of P phase. To measure the slowness of SKKKP signals, we computed vespagrams using a modified Nth root slant stack method[52]. Extended Data Fig. 4a,c,e,g,i shows the fourth-root vespagrams for the seismograms in Extended Data Fig. 3. The slownesses of the signals are clearly greater than 4.2 s per deg, confirming that they are SKKKP and its B-caustic diffractions. Moreover, a total of 17 available events were measured, and their slownesses are nearly constant at different distance ranges, with a discrepancy larger than 0.15 s per deg relative to B-caustic distance slowness (−4.37 s per deg) in only two cases (Supplementary Fig. 6a).

Beamforming method based on array data is a widely used technique in seismology to determine propagation direction of seismic waves[18,53]. We used data from the 17 events mentioned above to identify the travel paths of SKKKP B-caustic diffractions. Results show that 15 events have the back azimuth deviation less than 4° relative to the great circle path (Extended Data Fig. 4b,d,f,h,j and Supplementary Fig. 6b), implying that SKKKP B-caustic diffractions mainly propagate along the great circle path. The two cases with deviation greater than 4° indicate the complex interactions between SKKKP waves and strong lateral heterogeneities along the ray paths[15,18]. We then applied beamforming method for P waves, and the back azimuth deviations of the 17 events are all less than 3° (Supplementary Figs. 5 and 6b), suggesting that the strong lateral heterogeneities are in the lower mantle.

Testing the effects of slab structure anomalies

Previous studies have reported that notable seismic velocity anomalies within subducted slabs have the potential to distort waveforms[27,54]. This distortion can occur for seismic waves generated by earthquakes within the slab and propagating to teleseismic distances[55] and for teleseismic waves entering the slab and recorded by stations above the slab[56]. We used the SEM-DSM hybrid method[57] to test their effects on SKKKP B-caustic diffractions; this hybrid approach computes 3D wavefields at the boundaries of a source box using the spectral-element method[58] (SEM) and then propagates them to teleseismic distances based on the 1D direct solution method[59] (DSM). By confining the computationally expensive 3D simulations to a smaller source-side box, this method substantially reduces computational costs and, therefore, enables high-frequency (for example, 1 Hz or higher) 3D numerical simulations of teleseismic waves.

We incorporated simple slab structure models into the source-side SEM box and took the 20070716 M_b 6.2 earthquake as an example to test the slab effects. This earthquake occurred at a depth of 358.2 km in the subducted Pacific plate beneath Japan (Extended Data Fig. 5a) and exhibited a long-distance extension of SKKKP B-caustic diffractions (Fig. 2c). Three models of velocity anomalies in a thickness of 120 km slab were tested. The first model contains a top 7 km thick oceanic crust of low-velocity zone with a 10% reduction of S-wave and P-wave velocity. Below the oceanic crust is the subducting mantle with a 5% high-velocity anomaly, which linearly decays to the background 1D velocity downwards (Extended Data Fig. 5c). The second model includes two layers: the upper 37 km layer has a constant 5% high anomaly, and this anomaly linearly decays to the background velocity in the lower layer (Extended Data Fig. 5d). The third model has a triangular-shape velocity anomaly with a 5% anomaly peaking at the slab centre (Extended Data Fig. 5e).

The SEM box, centred at the 20070716 earthquake epicentre, has dimensions of 6° (longitude) × 6° (latitude) × 670 km (depth) (Extended Data Fig. 5b). To resolve 1.2 Hz waves, the SEM model is discretized with a mesh of 256 (longitude) × 256 (latitude) × 214 (depth) elements. The depth of the slab upper interface, obtained from the Slab2 model[28], serves as a reference for incorporating the slab structure models. We used the Global Centroid Moment Tensor (GCMT) solution for input source parameters and AK135 as the background 1D structure model. To reduce the computational cost, we extended the structure of lower crust upwards, replacing the upper crust characterized by lower velocities. It is noted that the truncated slab model is tapered at boundaries to reduce artificial reflections. We conducted the SEM simulation using a total of 256 Intel(R) Xeon(R) Gold 6140 CPU @ 2.30 GHz cores. Each individual simulation required approximately 23 hours, resulting in a total time of 69 hours for the three simulations.

1D and 2D synthetics

We used the AxiSEM software, a spectral-element method that simulates wave propagation in axisymmetric Earth models[60], to calculate 1D and 2D synthetic waveforms in this study. The dominant frequency of the synthetics is 0.75 Hz, and we focused on the modelling data in the 0.5–1.0 Hz frequency band. The software has been successfully used to study the various scales of complex structures in the deep Earth because of its high computational efficiency[8,61–63]. For simulating SKKKP wave propagation, we used the AK135 velocity model (avoiding the interference of P′210 P′) including an attenuation model from PREM[64] as the background model. The source parameters of the three events in Fig. 2 used in the simulations were obtained from the GCMT catalogue, and we used 20110902 M_b 6.4 earthquake for most synthetics. In addition, the MC Kernel method also utilized the forward and backward wavefield databases generated by AxiSEM at a dominant period of 4 s. Although SKKKP waves are better observed at approximately 0.8 Hz, saving wavefield databases at such high frequencies is still difficult.

Testing the effects of different ULVZ parameters

We tested a large set of 2D ULVZ models to better explore the influences of various ULVZ parameters on SKKKP B-caustic diffractions (Extended Data Table 2). First, we varied the shape and number of the ULVZ model (Supplementary Fig. 17). Synthetic results show that the extension lengths of SKKKP B-caustic diffractions are similar for ULVZ models with different shapes (sinusoid shaped and rectangle shaped). When we used three consecutive sinusoid-shaped ULVZ models on the receiver side, the extension length was even shortened, possibly due to the interference between B-caustic diffractions. We also tested three identical ULVZ models that were located at 107–108°, 109–110° and 111–112° from the earthquake epicentre at the CMB. The synthetic seismograms show that when the ULVZ model is closer to the B-caustic point (107.7° away from the earthquake epicentre), the time delays of SKKKP B-caustic diffractions increase and the extension lengths slightly shorten (Supplementary Fig. 18). For simplicity, we used a single sinusoid-shaped ULVZ model with constant S-wave velocity and density in the following modelling. For each test, we changed only one parameter of the ULVZ model, including the P-wave velocity reduction (2–20%), thickness (5–100 km) and width (30–600 km).

Extended Data Table 2 shows the extension lengths for different 2D ULVZ models in synthetic seismograms. We found that (1) effects of P-wave velocity reduction: SKKKP B-caustic diffractions are sensitive to the P-wave velocity reduction; the extension length increases with larger P-wave velocity reduction, but the increments become smaller and smaller (Extended Data Fig. 7). In addition, heterogeneities with increased P-wave velocity (UHVZ model[65]) can not effectively produce the continuous SKKKP waves as the ULVZ model. (2) Effects of ULVZ thickness: due to the limited resolution of SKKKP in the 0.5–1.0 Hz frequency band, the extension length is similar to that of the AK135 model when the thickness of the ULVZ model is less than 10 km. As the thickness reaches 20 km, the extension length stabilizes at 14° (Supplementary Fig. 19). (3) Effects of ULVZ width: as the width increases, the extension length first increases and then decreases (Supplementary Fig. 20), probably because SKKKP is less affected by the edge of the ULVZ model when the width is too large[66], just like the 1D ULVZ model. However, our simulations do not fully capture the effects of ULVZ edge due to the axisymmetric feature of the AxiSEM software. To explore the influences between different ULVZ parameters more accurately, true 3D simulation methods are necessary in the future[67].

Properties of ULVZs

Here we discuss the properties of ULVZs in different high-velocity lowermost mantle regions. The Central America region shows remarkable coverage by SKKKP B-caustic diffractions from events in the northwest Pacific. The extension lengths of different events range from 5° to 28°, indicating the complexity of ULVZs in this region. These ULVZs are expected to exhibit P-wave velocity reductions exceeding 6% and thicknesses greater than 20 km. Previous studies have detected several ULVZs in this region (Supplementary Fig. 23), and their parameters are consistent with our results. Niu and Wen[35] used PKP precursors to provide evidence for seismic scatters beneath the west of Mexico with dimensions of 200 km × 300 km and a P-wave velocity variation of at least 6%. In addition, using SPdKS waveforms, Thorne et al.[5] identified that there are at least three ULVZs at the CMB beneath northern Mexico and the southeastern United States. Waveform modelling suggests that the ULVZs feature P-wave velocity reductions of 10% and thicknesses of more than 20 km. The SKKKP B-caustic diffractions from South America events provide sampling for the Alaska region, and our preferred models are ULVZs with a P-wave velocity reduction of 8% and a thickness of 30 km at the CMB. The Greenland and West and Central Asia regions both show dense sampling by SKKKP B-caustic diffractions from events in the Fiji–Tonga region. The common feature of B-caustic diffractions in these regions is the long-distance extension (greater than 18°), suggesting that the P-wave velocity reductions of the ULVZs are greater than 12%.

Data availability

Most waveform data were downloaded using ObsPy[68] from the Incorporated Research Institutions for Seismology Data Management Center (http://service.iris.edu), the Southern California Earthquake Data Center (https://scedc.caltech.edu), the GEOFON data centre of the GFZ German Research Centre for Geosciences (http://geofon.gfz-potsdam.de), the Italian National Institute of Geophysics and Volcanology (http://webservices.ingv.it) and the following networks (described by their network codes): GR (https://doi.org/10.25928/mbx6-hr74), RN (https://doi.org/10.7914/SN/RN), SX (https://doi.org/10.7914/SN/SX), TH (https://doi.org/10.7914/SN/TH), NO (http://fdsn.org/networks/detail/NO), NS (http://fdsn.org/networks/detail/NS), KO (https://doi.org/10.7914/SN/KO). Other waveform data were downloaded under license from the International Earthquake Science Data Center (https://doi.org/10.11998/IESDC). Earthquake information in Supplementary Tables 1–4 was obtained from the ISC earthquake catalogue search engine (http://www.isc.ac.uk/iscbulletin/search/catalogue). Source parameters of the three events in Fig. 2 were obtained from the GCMT catalogue (https://www.globalcmt.org). Tomographic models used in this study are accessible through the references provided[29–33]. The source data for Figs. 1–4 and Extended Data Figs. 1–8, information on event–station pairs and waveform data from International Earthquake Science Data Center in this study can be accessed at https://doi.org/10.6084/m9.figshare.24465991. Source data are provided with this paper.

Code availability

The synthetic seismograms were generated by the open source AxiSEM (http://seis.earth.ox.ac.uk/axisem) and SEM-DSM hybrid method (https://github.com/wenbowu-geo/SEM_DSM_hybrid). The finite-frequency sensitivity kernels were calculated using open source MC Kernel (http://seismology.github.io/mc_kernel). The waveform analyses were done using the ObSpy[68]. Figures were created using GMT (https://www.generic-mapping-tools.org). Specific data processing and figure plotting scripts are available from the corresponding author upon request.

References

51. Haddon, R. A. W., Husebye, E. S. & King, D. W. Origins of precursors to P′P′. *Phys. Earth Planet. Inter.* **14**, 41–70 (1977).
52. Rost, S. & Thomas, C. Array seismology: methods and applications. *Rev. Geophys.* **40**, RG000100 (2002).

53. Wu, W., Ni, S. & Irving, J. C. E. Inferring Earth's discontinuous chemical layering from the 660-kilometer boundary topography. *Science* **363**, 763–740 (2019).
54. Abers, G. A. Seismic low-velocity layer at the top of subducting slabs: Observations, predictions, and systematics. *Phys. Earth Planet. Inter.* **149**, 7–29 (2005).
55. Zhan, Z., Helmberger, D. & Li, D. Imaging subducted slab structure beneath the Sea of Okhotsk with teleseismic waveforms. *Phys. Earth Planet. Inter.* **232**, 30–35 (2014).
56. Frost, D. A., Romanowicz, B. & Roecker, S. Upper mantle slab under Alaska: contribution to anomalous core-phase observations on south-Sandwich to Alaska paths. *Phys. Earth Planet. Inter.* **299**, 106427 (2020).
57. Wu, W., Ni, S., Zhan, Z. & Wei, S. An SEM-DSM three-dimensional hybrid method for modelling teleseismic waves with complicated source-side structures. *Geophys. J. Int.* **215**, 133–154 (2018).
58. Komatitsch, D. & Tromp, J. Introduction to the spectral element method for three-dimensional seismic wave propagation. *Geophys. J. Int.* **139**, 806–822 (1999).
59. Kawai, K., Takeuchi, N. & Geller, R. J. Complete synthetic seismograms up to 2 Hz for transversely isotropic spherically symmetric media. *Geophys. J. Int.* **164**, 411–424 (2006).
60. Nissen-Meyer, T. et al. AxiSEM: broadband 3-D seismic wavefields in axisymmetric media. *Solid Earth* **5**, 425–445 (2014).
61. Hosseini, K. & Sigloch, K. Multifrequency measurements of core-diffracted P waves (Pdiff) for global waveform tomography. *Geophys. J. Int.* **203**, 506–521 (2015).
62. Jenkins, J., Mousavi, S., Li, Z. & Cottaar, S. A high-resolution map of Hawaiian ULVZ morphology from ScS phases. *Earth Planet. Sci. Lett.* **563**, 116885 (2021).
63. Russell, S., Irving, J. C. & Cottaar, S. Seismic visibility of melt at the core–mantle boundary from PKKP diffracted waves. *Earth Planet. Sci. Lett.* **595**, 117768 (2022).
64. Dziewonski, A. M. & Anderson, D. L. Preliminary reference Earth model. *Phys. Earth Planet. Inter.* **25**, 297–356 (1981).
65. Garnero, E. et al. Ultra high velocity zones at the core–mantle boundary. *American Geophysical Union, Fall Meeting* Abstr. DI008-05 (2020).
66. Vanacore, E., Niu, F. & Ma, Y. Large angle reflection from a dipping structure recorded as a PKIKP precursor: Evidence for a low velocity zone at the core-mantle boundary beneath the Gulf of Mexico. *Earth Planet. Sci. Lett.* **293**, 54–62 (2010).
67. Yuan, K. & Romanowicz, B. Seismic evidence for partial melting at the root of major hot spot plumes. *Science* **357**, 393–397 (2017).
68. Beyreuther, M. et al. ObsPy: a Python toolbox for seismology. *Seismol. Res. Lett.* **81**, 530–533 (2010).

Acknowledgements

All maps in this paper were produced using GMT developed by P. Wessel and W.H.F. Smith. We thank T.T. Cao for helping with the cartoon in Fig. 4. This study is supported by National Natural Science Foundation of China (42030311 received by S.N., 42274077 received by B.Z., 42394114 received by M.H.), the Strategic Priority Research Program (B) of the Chinese Academy of Sciences (grant number XDB41000000 received by B.Z.).

Author contributions

S.N. conceived the study. Y.S. analysed the data, prepared the figures and drafted the paper under the supervision of S.N. and B.Z. Y.S. and W.W. performed the synthetics. Y.S. and Y.C. calculated the sensitivity kernels. M.L. contributed to geodynamical interpretations and paper preparation. D.S. and W.W. provided guidance on seismological results. H.S., M.H. and X.C. contributed to the discussion of conclusions. All authors discussed the results and contributed to writing the paper.

Competing interests

The authors declare no competing interests.

Additional information

Extended data is available for this paper at https://doi.org/10.1038/s41561-024-01394-5.

Supplementary information The online version contains supplementary material available at https://doi.org/10.1038/s41561-024-01394-5.

Correspondence and requests for materials should be addressed to Sidao Ni.

Peer review information *Nature Geoscience* thanks the anonymous reviewers for their contribution to the peer review of this work. Primary Handling Editors: Alireza Bahadori and Stefan Lachowycz, in collaboration with the *Nature Geoscience* team.

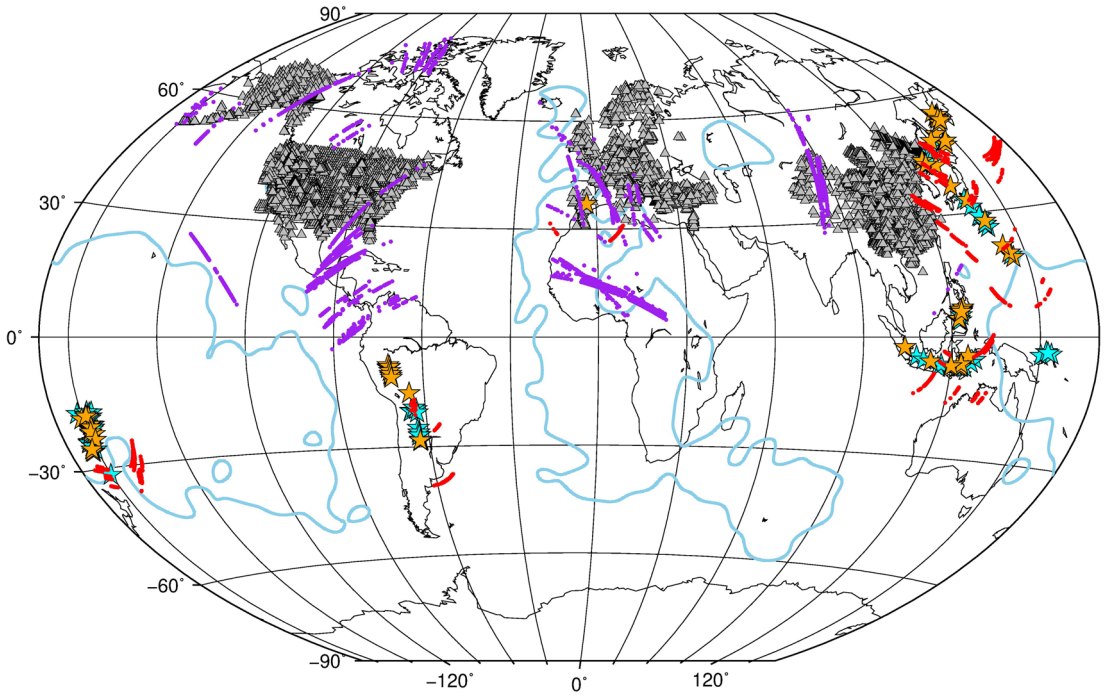

Extended Data Fig. 1 | Distribution of events and stations used in this study. A total of 143 events (stars) with a magnitude of more than M_b 6.0 and a depth of more than 300 km recorded by broad-band and short-period stations (triangles) were used for SKKKP B-caustic diffractions analyses. The events that show SKKKP or its B-caustic diffractions are marked with orange stars, while the events that do not show these seismic waves are marked with cyan stars. The red points and purple points indicate the theoretical core entry point and core exit point at B-caustic distance for event-station pairs with SKKKP B-caustic diffractions. The contours are drawn for reference at the −0.5% S-wave velocity level from tomographic model S40RTS at a depth of 2,850 km.

https://doi.org/10.1038/s41561-024-01394-5

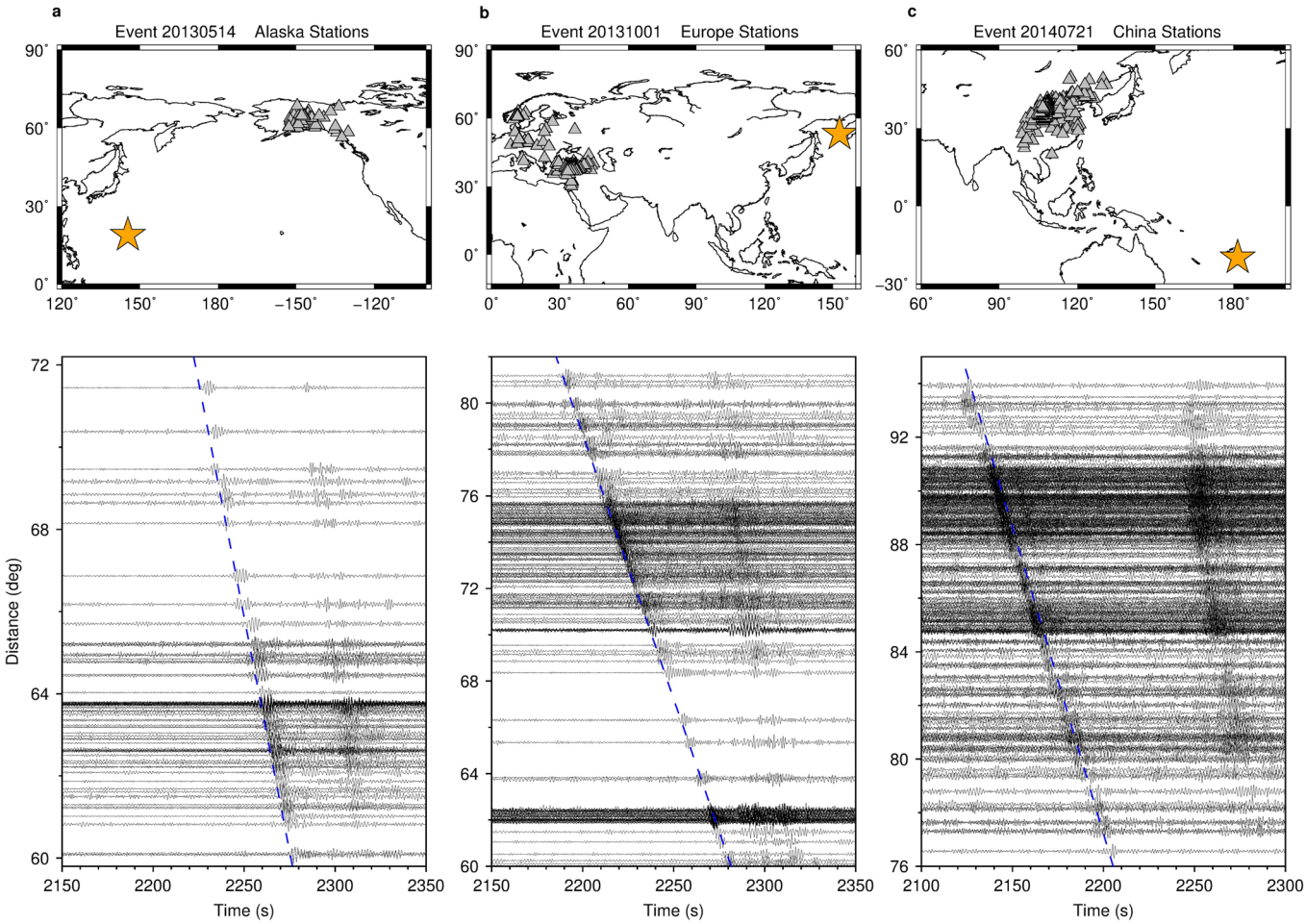

Extended Data Fig. 2 | Observations of SKKKP and its B-caustic diffractions. **a-c**, Record sections display vertical component seismograms in the frequency band 0.5–1.2 Hz for three deep-focus events. **a**, The 20130514 event, magnitude M_b 6.2, depth 611.7 km. **b**, The 20131001 event, magnitude M_b 6.3, depth 578.4 km. **c**, The 20140721 event, magnitude M_b 6.4, depth 614.0 km. The dashed blue lines show the theoretical travel time curves of SKKKP and its B-caustic diffractions calculated with the AK135 model using a constant slowness of −4.37 s per deg. The maps above the record sections show the locations of events (orange stars) and stations (grey triangles).

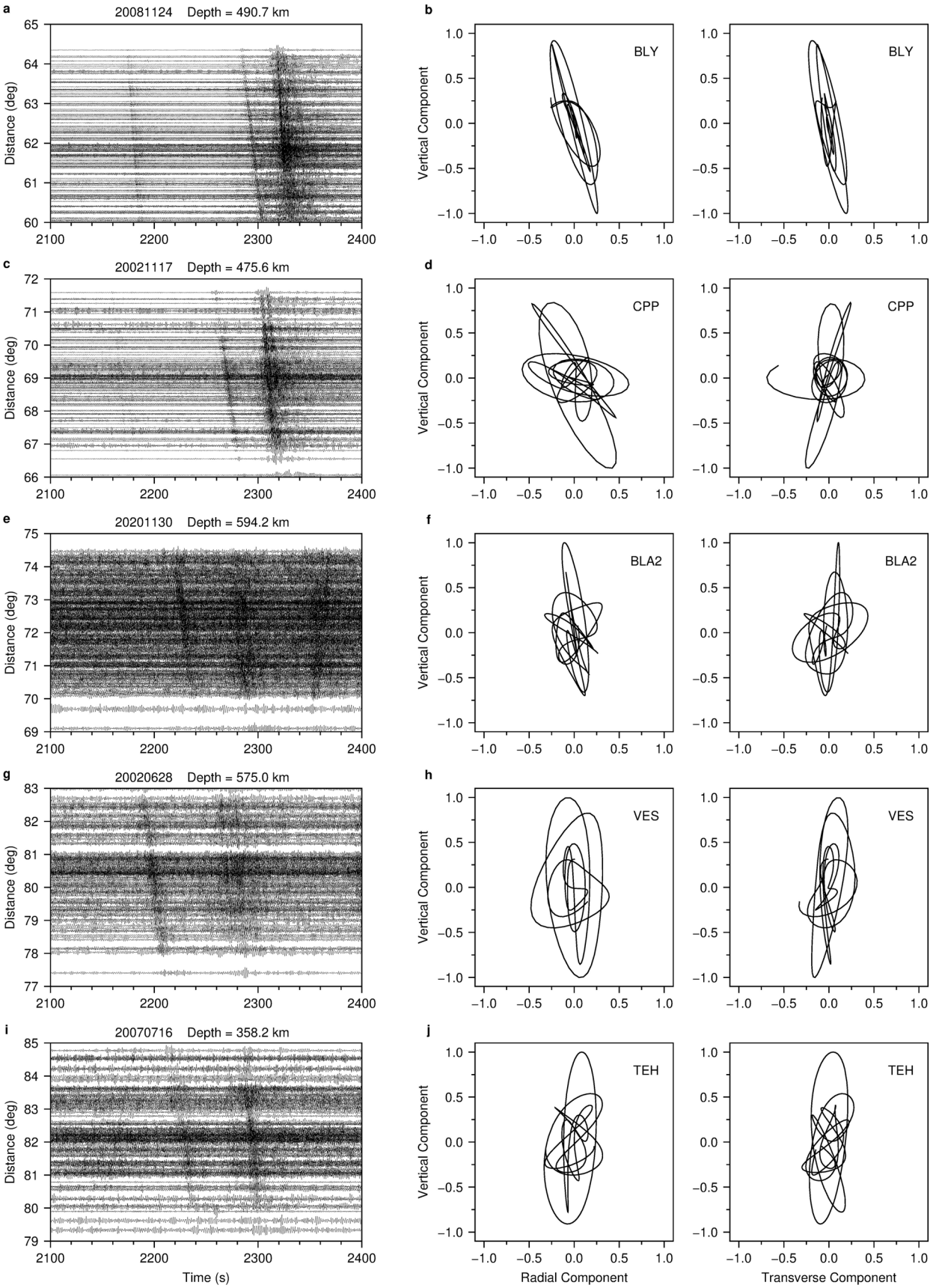

Extended Data Fig. 3 | Record sections and particle motions of SKKKP and its B-caustic diffractions from the Southern California Seismic Network. **a**,**c**,**e**,**g**,**i**, Record sections show vertical component seismograms in the frequency band 0.5–1.2 Hz for five deep-focus events at different epicentral distance ranges. **b**,**d**,**f**,**h**,**j**, Particle motions at one of the stations of the record section on the left with a high signal-to-noise ratio.

https://doi.org/10.1038/s41561-024-01394-5

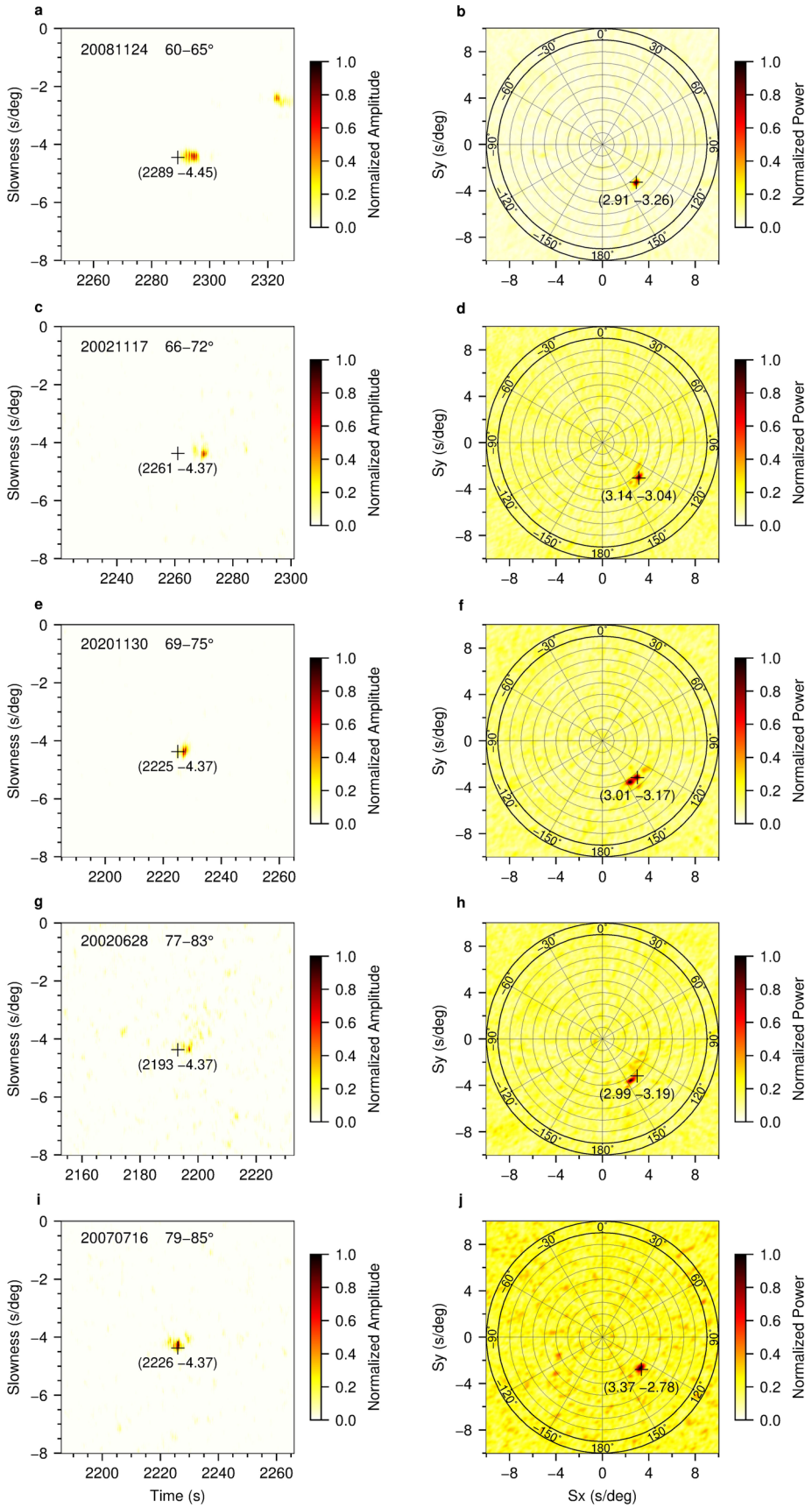

Extended Data Fig. 4 | Vespagrams and beamforming results of SKKKP and its B-caustic diffractions. a,**c**,**e**,**g**,**i**, Fourth-root vespagrams of the seismograms shown in Extended Data Fig. 3. The black crosses indicate the theoretical arrival times and slownesses for SKKKP or its B-caustic diffractions calculated with the AK135 model. **b**,**d**,**f**,**h**,**j**, Beamforming results of the seismograms shown in Extended Data Fig. 3. The black crosses indicate the theoretical slownesses and back azimuths for SKKKP or its B-caustic diffractions calculated with AK135 model.

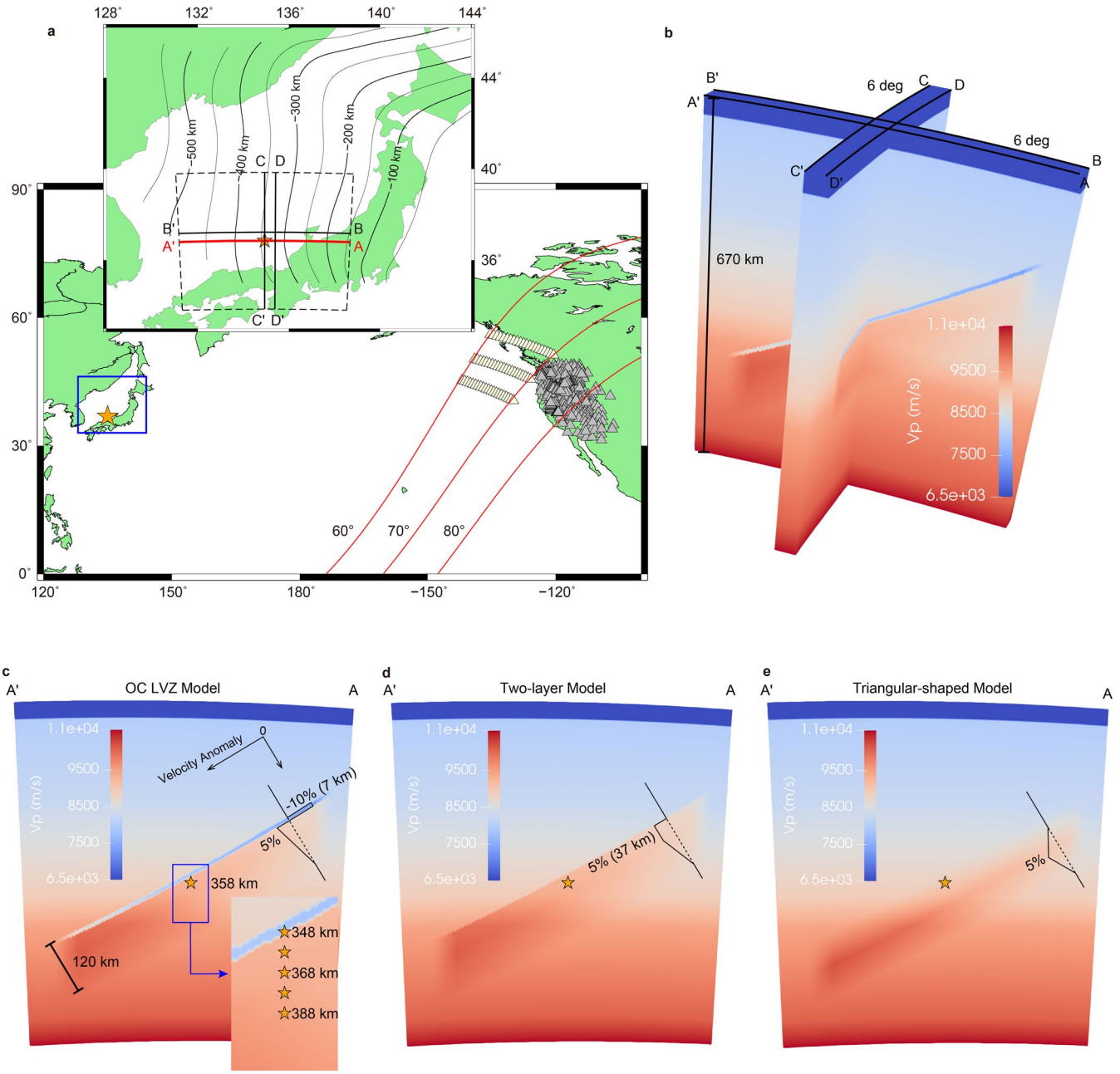

Extended Data Fig. 5 | Map and SEM model set-up for testing the effects of slab structure anomalies. a, The large map shows the locations of the 20070716 event (M_b 6.2, depth 358.2 km, orange star), real stations (grey triangles) and added stations (light-yellow triangles) that were used for the synthetic test. The red lines represent the epicentral distance contours. The small map displays the magnified area of the blue box in the large map. The solid black lines represent the depth contours of the slab. **b**, The cross-shaped slice (A-A′, B-B′, C-C′ and D-D′ in **a**) of the 6° (longitude) × 6° (latitude) × 670 km (depth) SEM box (the dashed black box in **a**). **c**-**e**, The depth profiles of P-wave velocity along the slab downdip direction (A-A′ in **a**). The slab has a thickness of 120 km and the black lines in **c**-**e** show the velocity anomaly of the slab. The inset in **c** shows the location of earthquakes at different depths in synthetic tests that use the same OC LVZ model.

https://doi.org/10.1038/s41561-024-01394-5

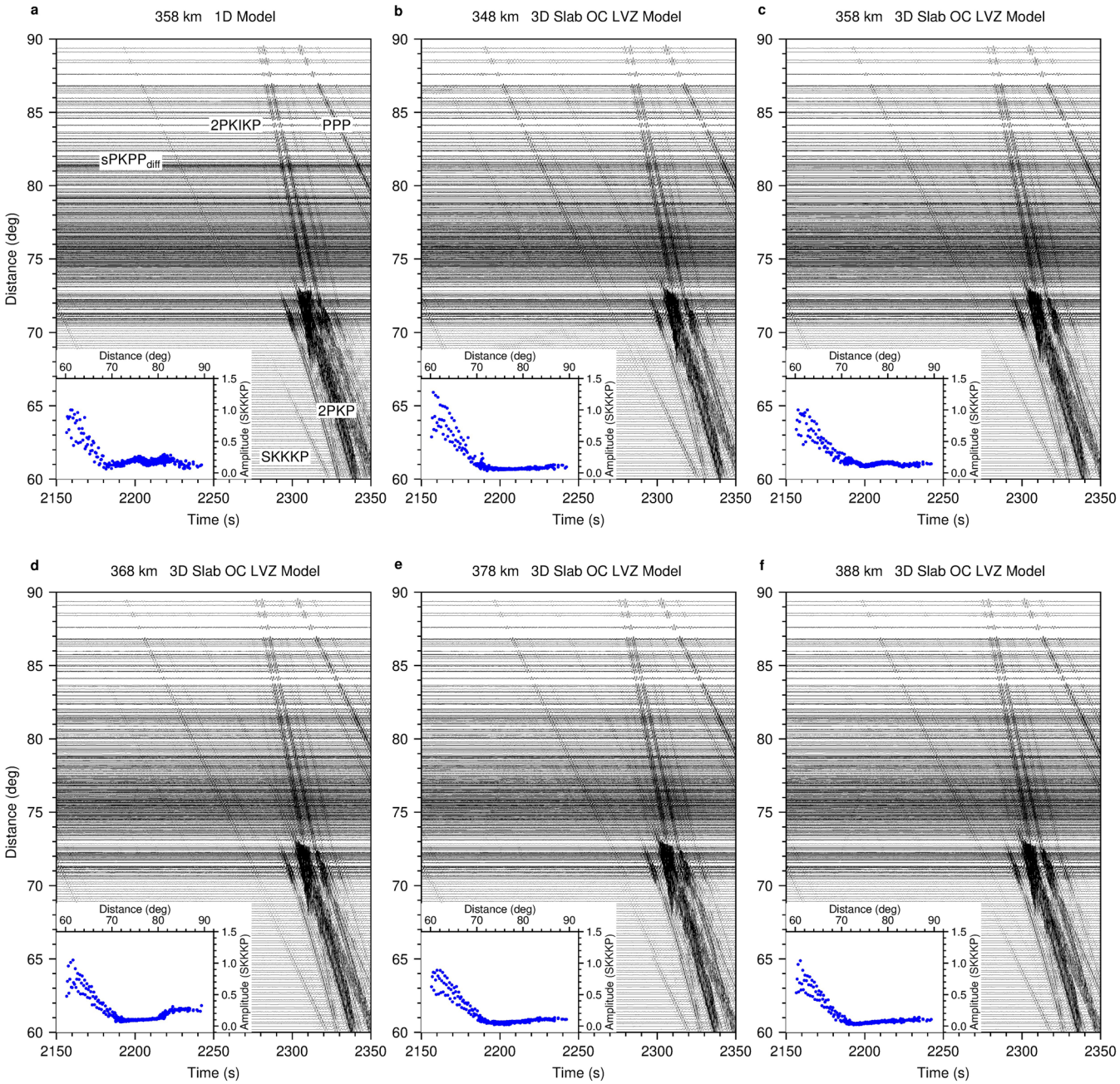

Extended Data Fig. 6 | Distance profiles for 1D model and 3D slab models with different focal depths. a, 1D synthetics with AK135 model. **b**-**f**, 3D synthetics generated by varying the depth of the earthquake while using the same OC LVZ model in Extended Data Fig. 5c. The source depths are 348 km (**b**), 358 km (**c**), 368 km (**d**), 378 km (**e**) and 388 km (**f**). The insets in **a**-**f** show the amplitude of SKKKP versus epicentral distance. All the waveforms are filtered with 0.5–1.0 Hz.

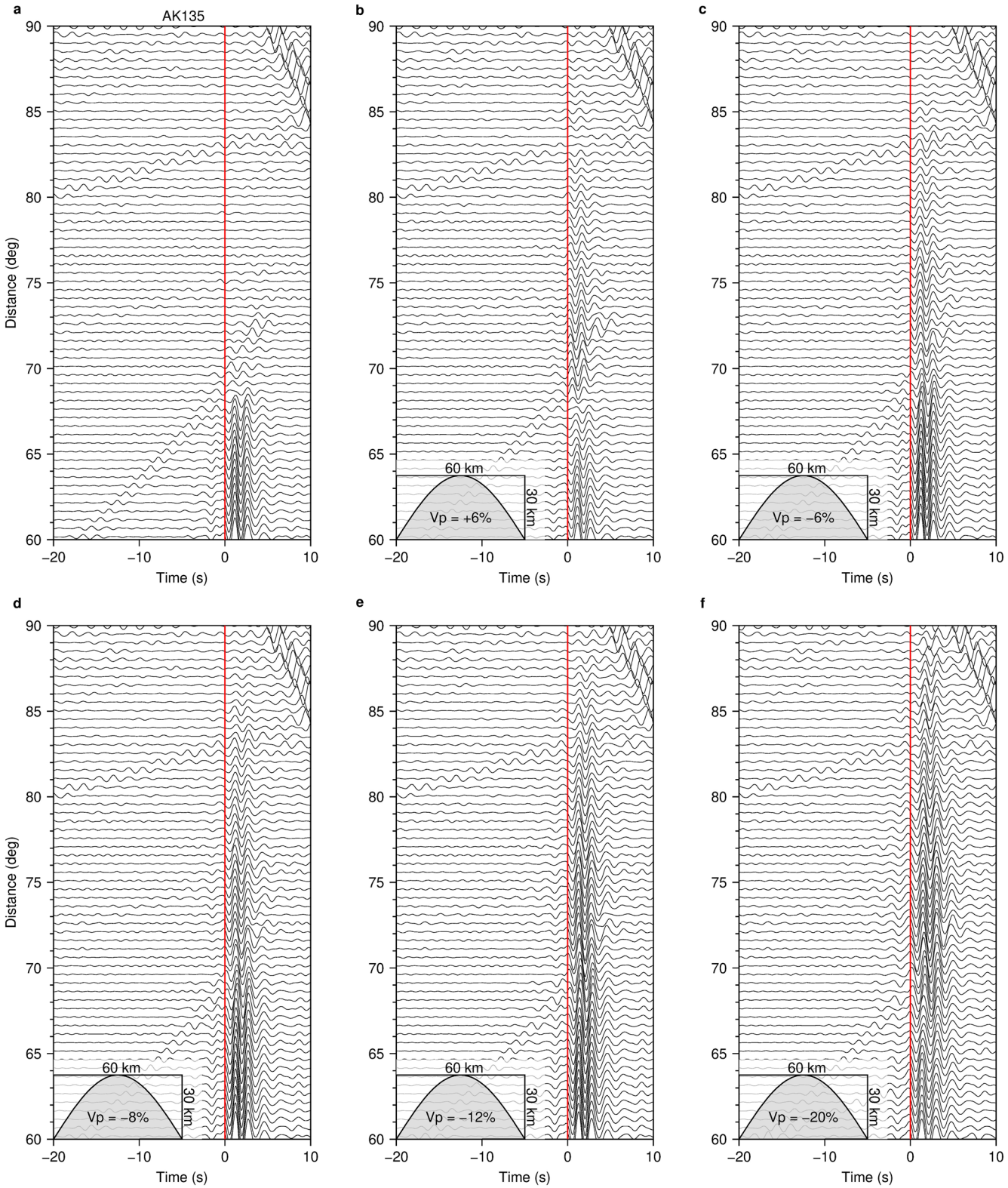

Extended Data Fig. 7 | Synthetic seismograms for 1D model and 2D ULVZ models with different P-wave velocity variations on the receiver side. a, AK135 model. **b-f**, 2D sinusoid-shaped ULVZ models with a thickness of 30 km, a width of 60 km, and a P-wave velocity increase of 6% (**b**), a P-wave velocity reduction of 6% (**c**), a P-wave velocity reduction of 8% (**d**), a P-wave velocity reduction of 12% (**e**), a P-wave velocity reduction of 20% (**f**). All the waveforms are aligned with the theoretical arrival times of SKKKP and its B-caustic diffractions (red lines) and filtered with 0.5–1.0 Hz.

https://doi.org/10.1038/s41561-024-01394-5

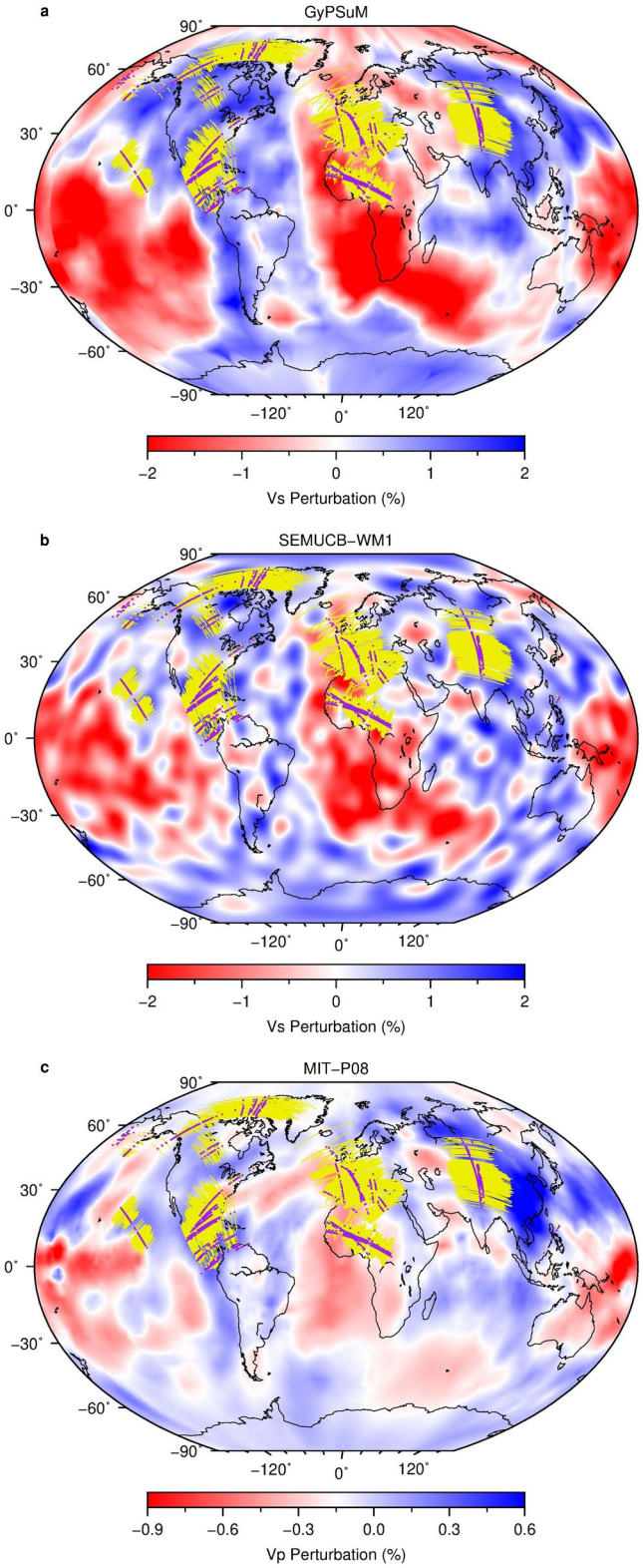

Extended Data Fig. 8 | Sampling regions of SKKKP B-caustic diffractions. **a-c**, Locations of the sampling regions on different tomographic models. The background models display S-wave velocity tomographic model GyPSuM (**a**), SEMUCB-WM1 (**b**) and P-wave velocity tomographic model MIT-P08 (**c**). Yellow lines indicate the potential sampling regions of SKKKP B-caustic diffractions at the CMB, and their lengths represent the extension lengths. The purple points represent the theoretical core exit point of SKKKP at B-caustic distance for event-station pairs.

Extended Data Table 1 | Parameters of 1D anomalous velocity models near the CMB region

Model	Type of Velocity Change	P-wave Velocity	S-wave Velocity	Thickness	Depth Range
AK135	\	\	\	\	\
1D ULVZ1	Sharp	–8%	\	30 km	30 km above CMB
1D ULVZ2	Sharp	\	-24	30 km	30 km above CMB
1D ULVZ3	Sharp	–5%	–15%	50 km	50 km above CMB
LVZ1	Gradual	–3%	\	150 km	150 km above CMB
LVZ2	Sharp	–3%	\	150 km	150 km above CMB
LVZ3	Gradual	\	–5%	150 km	150 km above CMB
HVZ1	Gradual	+3%	\	150 km	150 km above CMB
HVZ2	Sharp	+3%	\	150 km	150 km above CMB
HVZ3	Gradual	\	+5%	150 km	150 km above CMB
Molten Layer1	Sharp	–30%	\	5 km	5 km above CMB
Molten Layer2	Gradual	–10%	\	10 km	10 km above CMB
Molten Layer3	Sharp	–5%	–15%	5 km	5 km above CMB
CRZ	\	Vp=10 km/s	Vs=0.7 km/s	1 km	1 km below CMB
OC Top1	Gradual	–0.02 km/s	\	100 km	100 km below CMB
OC Top2	Gradual	–0.04 km/s	\	200 km	200 km below CMB
OC Top3	Gradual	–0.08 km/s	\	300 km	300 km below CMB
OC Top4	Gradual	+0.08 km/s	\	300 km	300 km below CMB

https://doi.org/10.1038/s41561-024-01394-5

Extended Data Table 2 | Extension lengths of SKKKP B-caustic diffractions for 2D ULVZ models with different parameters on the receiver side

P-wave Velocity	Thickness (km)	Width (km)	Location (deg)	Extension Length (deg)
-2%	30	60	109-110	2
-4%	30	60	109-110	4
-6%	30	60	109-110	10
-8%	30	60	109-110	14
-10%	30	60	109-110	17
-12%	30	60	109-110	19
-20%	30	60	109-110	21
-8%	5	60	109-110	2
-8%	10	60	109-110	4
-8%	20	60	109-110	14
-8%	30	60	109-110	14
-8%	40	60	109-110	14
-8%	50	60	109-110	14
-8%	70	60	109-110	14
-8%	100	60	109-110	14
-8%	30	30	109.3-109.8	6
-8%	30	60	109-110	14
-8%	30	120	108.5-110.5	16
-8%	30	180	108-111	14
-8%	30	240	107.5-111.5	13
-8%	30	300	107-112	12
-8%	30	600	105-115	9
-8%	30	60	107-108	12
-8%	30	60	109-110	14
-8%	30	60	111-112	14
-8%	30	180	106-109	14
-8%	30	180	108-111	14
-8%	30	180	110-113	14